We are IntechOpen,
the world's leading publisher of Open Access books
Built by scientists, for scientists

6,900
Open access books available

186,000
International authors and editors

200M
Downloads

Our authors are among the

154
Countries delivered to

TOP 1%
most cited scientists

12.2%
Contributors from top 500 universities

BOOK CITATION INDEX
CLARIVATE ANALYTICS
INDEXED

WEB OF SCIENCE™

Selection of our books indexed in the Book Citation Index
in Web of Science™ Core Collection (BKCI)

Interested in publishing with us?
Contact book.department@intechopen.com

Numbers displayed above are based on latest data collected.
For more information visit www.intechopen.com

SiC Devices on Different Polytypes: Prospects and Challenges

Moumita Mukherjee

Centre for Millimeter-Wave Semiconductor Devices and Systems (CMSDS), Institute of Radio Physics and Electronics, University of Calcutta, West Bengal, India

1. Introduction

Imaging, broadband communication and high-resolution spectroscopic applications in the mid- and far-infrared regions have underscored the importance of developing reliable solid-state sources operating in the frequency range from 0.3 Terahertz to 10.0 Terahertz (1000 to 30 µm wavelength). Recent studies suggest that Terahertz (THz) interactions can enable a variety of new applications on the wide range of solids, liquids, gases, including polymers and biological materials such as proteins and tissues. Compared to microwave and MM-wave, far-infrared or THz frequency range has significant reduction in the antenna sizes and greater communication bandwidth. Commercial applications comprise thermal imaging, remote chemical sensing, molecular spectroscopy, medical diagnosis and surveillance. Military applications comprise night vision, rifle sight enhancement, missile tracking, space based surveillance and target recognition. Despite the technical advantages, the major challenge today in THz technology is the development of a portable high-power THz source. During the past few years, significant efforts were devoted to search of reliable semiconductor sources at the THz regime.

Recently, several solid-state physics research group, the world over, are focusing their research attention in developing semiconductor devices those can generate THz oscillations. A promising concept for THz sources utilizing plasma waves in a gated 2D electron gas (2DEG) was proposed in the early 90-ties. Thereafter, recent experimental observations and theoretical studies have revealed that resonant detection and coherent emission of THz radiation can be effectively induced by excitation of plasma oscillations in the electron channel of Field Effect Transistors (FET). Another promising THz source is the Quantum Cascade Laser (QCL). QCL were first demonstrated in 1994 based on a series of coupled quantum wells constructed using MBE. Although in the mid-infrared region ($5 < \lambda < 10$ µm) these devices have been in development for more than ten years, it is only recently that the first THz laser has been reported at 4.4 THz. These lasers are made from 1,500 alternating layers of GaAs and AlGaAs and have produced 2.0 mW of peak power (20.0 nW average power). Advances in output power and operating wavelength continue at a rapid pace. Low Temperature Grown (LTG) GaAs photo-mixer can provide up to around 2µW of output power at the frequency of 1.0 THz and their operation frequency can be as high as 5 THz. Of the several available terahertz source technologies, those based on the difference frequency technique are very promising, as they can produce a relatively high power terahertz beam

over the frequency from 100 GHz to 3.5 THz, which is tunable. Recently THz output power level exceeding 10 mW (occasionally 100 mW) at the frequency of around 1.0 THz has been demonstrated with a special type of electro-optically tunable compact terahertz source.

It is clear from the brief review that the commercially available recent THz sources are complex and bulky. It will be more useful if THz frequency oscillation can be generated from a small sized single solid state source. Among all the two terminal solid state sources, IMPATT diodes have already been established as the most efficient semiconductor sources that can generate highest MM-wave power. Conventional Si and GaAs based IMPATT diodes were found to be reliable but they are limited by power and operating frequencies due to the limitation imposed by their inherent material parameters. WBG semiconductor such as Silicon Carbide (SiC) has received remarkable attention during the last decade as a promising device material for high-temperature, high-frequency and high- power device applications due to its high thermal conductivity, high saturation velocity of charge carriers and high critical field for breakdown. SiC exhibits higher value of thermal conductivity (3-10 times), critical electric field (5-10 times) and saturated carrier velocity (~ 2 times) compared to the conventional semiconductor materials such as Si and GaAs. For a better comparison of the possible high-power, high-frequency performances of these materials, some commonly knew FOMs (Figure of Merit). Taking *Keyes'* and *Johnson's* FOM for Si as unity, the *Keyes'* and *Johnson's* FOM for GaAs are 0.45 and 7.1, respectively, while those for SiC are 5.1 and 278. From the FOMs for high-frequency and high-temperature operation, SiC appears to be superior to both Si and GaAs.

SiC crystallizes in numerous polytypes. The three most common polytypes are the cubic phase, 3C and the hexagonal phases, 4H, and 6H-SiC. The cubic structure, referred to as β-SiC, is expected to have the highest saturation drift velocity. However, the energy bandgap of the 3C phase is significantly smaller than either the 4H or 6H phases, implying a lower breakdown voltage. In addition to this, β-SiC is difficult to grow in a mono-crystalline form due to its meta-stability resulting in a solid-state transformation into an alpha (α)-structure. Due to difficulty in the growth of β-SiC, most of the efforts for producing bulk mono-crystalline growth have concentrated on the more easily prepared α-polytypes, referred to as 4H-SiC and 6H-SiC. Thus due to the availability and quality of reproducible single-crystal wafers in these polytypes, 4H- and 6H-SiC-based electronic devices presently exhibit the most promise. The energy band gap of >3.0 eV in hexagonal (4H and 6H) SiC enables the devices based on such materials, to support peak internal electric field (E_c) about ten times higher than Si and GaAs. Higher E_c increases the breakdown voltage, an essential criterion for generation of high output power in a device. Higher E_c also permits incorporation of higher doping level in the depletion layer of the device, which in turn, reduces the width of the active region. Thus the device layers can be made very thin. The transit times of carriers become very small in a thin layered semiconductor if the carrier drift velocities are high. The intrinsic material parameters of hexagonal SiC are thus favorable for the realization of high-power devices.

2. History of IMPATT devices

A device possesses negative resistance when the A.C. current lags the voltage by a phase angle between 90° and 270°. The negative resistance in an avalanche diode occurs as a result of 180° phase difference between the A.C. current and voltage in a p–n junction reverse–biased to avalanche breakdown. The phase difference is produced by the time delay

inherent in the build–up of the avalanche current, coupled with the phase delay developed as the carriers traverse the depletion layer. The word IMPATT stands for "impact ionization avalanche transit time". IMPATT diodes employ impact–ionization and transit–time properties of semiconductor structures to produce negative resistance at microwaves and millimeter waves frequencies. The negative resistance arises from two delays which cause the current to lag behind the voltage. One is the 'avalanche delay' caused by finite buildup time of the avalanche current; the other is the 'transit–time delay' caused by the finite time required by the carriers to cross the "drift" region. When these two delays add up to half–cycle time, the diode electronic resistance is negative at the corresponding frequency. IMPATT devices have emerged as most powerful solid-state devices for generation of high CW and pulsed power at millimeter wave frequencies. These devices also provide high oscillator output power with high DC to RF conversion efficiency in Silicon Monolithic Millimeter Wave Integrated Circuits (SIMMWIC).

In a practical mm-wave IMPATT oscillator the diode is embedded in a circuit which is resonant at a frequency within the negative–resistance band of the device. The oscillation is initiated by random noise fluctuations, which grows in a negative–resistance medium at the resonant frequency of the circuit. In practice the device has to be mounted either in a coaxial line or in a section of wave-guide or in a micro strip circuit.

In 1954, Schokley first studied the microwave negative resistance from the transit time delay of an electron bunch in a forward biased p-n junction diode. Afterwards, in 1958, W. T. Read showed that the finite delay between an applied RF voltage and the external current is due to the generation of carriers in a reverse biased p+-n i n+ diode under avalanche breakdown and the subsequent drift of carriers through the depletion layer. This would lead to a negative resistance of the device at microwave frequencies. In 1965, Johnston et al experimentally observed microwave oscillation from a simple p+nn+ device. At the same time Lee et al also reported oscillation at microwave frequency from a Read diode. Small signal analysis of avalanche diodes of general doping profiles was carried out by T. Misawa, who showed that the negative resistance occurs in any reverse biased p-n junction diode of arbitrary doping profile.

In 1968 Lee et al first reported resonant-cap mounted IMPATT oscillator together with a simplified equivalent circuit. Their report showed CW power of 100 mW at 50 GHz with an overall efficiency of 2 percent. In the same year Misawa [9] reported millimeter-wave oscillation from silicon avalanche diode with abrupt junction mounted in a resonant-cap waveguide circuit. His report shows a CW output power in the range of 23 to 150 mW for the 50 to 84 GHz frequency range with a maximum efficiency of 3 percent. In 1970, Misawa and Kenyon reported mechanical tuning characteristics of resonant-cap IMPATT oscillators at millimeter-wave frequencies. Since then , fast advances in semiconductor technology , rapid advances have been made towards further development of various IMPATT diode structures as well as IMPATT based oscillators and amplifiers to meet the to-days high power requirement in higher frequency band. In recent years lot of interest has been created regarding IMPATT diodes and oscillators based on SiC as a semiconducting material. Considerable advancement regarding device physics, device fabrication and the optimum circuit design for IMPATT oscillator and amplifiers has push the frequency range to mm and sub mm regions which has resulted in the emergence of IMPATTs the most powerful solid state devices for generation of microwave and mm wave power.

To understand the operation and performance of IMPATT devices and oscillators knowledge of the basic IMPATT phenomena is required and briefly discussed in the following section. To build an IMPATT oscillator the device has to be mounted in a suitable microwave/mm-wave circuits. The performance of the oscillator strongly depends not only on the device but also on the circuit in which the device is embedded .The various microwave/mm-wave circuits that are being widely used to construct IMPATT oscillators have been reviewed briefly.

A brief review of the fundamental physical processes involved in IMPATT action followed by a review of the various IMPATT structures and oscillators will be presented in this section. The factors, which determine the avalanche delay and the transit time delay for high frequency operation of IMPATT will also be briefly discussed.

2.1 High field properties of charge carriers in IMPATT devices

The different scattering interactions between the charge carriers and the lattice lead to the emission of both acoustic and optical phonons which give rise to the saturation of carrier's drift velocity in semiconductors which is one of the fundamental physical phenomenon involved in IMPATT action.

Drift velocity of charge carriers has been observed to be linear upto the electric field 104 V.m-1 and it reaches a scattering limited value independent of the electric field when the field is very high ($>10^6$ V.m^{-1}). At low values of electric field (E), which the principal scattering phenomenon is acoustic phonon,   the drift velocity (v_d) of charge carriers in semiconductor varies as :

$$v_d = \mu_o E \tag{1}$$

Where μ_o is the low field mobility and can be expressed as,

$$\mu_o = \frac{q <v^2 \tau_o>}{m^* <v^2>} \tag{2}$$

Where q is the charge of the electron, m* is the effective mass of the carrier, τ_o is the relaxation time and v is the carrier velocity. The brackets in the above expression indicate Maxwellian average.

In the low field region (Ohmic region), the rate of energy through acoustic phonon collision is small and the scattering is isotropic. Assuming energy distribution to be Maxwellian at lattice temperature T and a constant mean free path, the low field mobility is given by,

$$\mu_o = \frac{4ql_a}{3(2\pi m^* KT)^{0.5}} \tag{3}$$

Where la is the mean free path for acoustic phonon collision and K is the Boltzman constant. At high electric field ($>10^6$ V.m^{-1}) high-energy electrons (hot electrons) interact more strongly with lattice and there is a departure from the linear dependence of drift velocity with the electric field. The thermal equilibrium is lost because the rate of energy gained from the field is more that the amount lost to the crystal lattice through low energy acoustic phonon collision.   At this high field, emission of optical phonons is a dominant phenomenon, which are quanta of high frequency thermal vibrations of the lattice in which

two face centered cubic sub lattices of the crystal vibrate in the opposite directions. Excitation of the optical phonons are possible when the electrons gain a minimum energy equal to optical phonon energy or Ramam energy $\varepsilon_{op} = (\frac{h}{2\pi})\omega_o$, where ω_o is the angular frequency for optical mode of vibration and h is the Planck's constant. The values of ε_{op} for GaAs and Silicon are obtained from neutron scattering experiments [18-21] and are of the order of 0.035 eV and 0.063 eV respectively. At a high field (>107 V.m-1), the average carrier kinetic energy exceeds the optical phonon energy ε_{op} and thereby a transfer of energy to the lattice via optical phonon is created and reaches a scattering limited average drift velocity independent of the electric field and is given by,

$$v_d = [\frac{8\varepsilon_{op}\tanh(\varepsilon_{op}2KT)}{3\pi m*}]^{0.5}$$ (4)

Drift velocity of carriers in Si at different field has been accurately determined by a number of workers using the time of flight technique and the space charge resistance technique [23-26]. The time of flight technique provides direct measurement of the drift velocity of both majority and minority carriers accurately. In 1967, Duh and Moll measured the carrier drift velocity in Si at high electric field (> 10⁷ V.m-1) and it shows that a slow increase of vd in the field range (2.6 - 4.35)x107 V.m-1. At a high field (2x10⁷ V.m-1) impact ionization becomes an important scattering mechanism in addition to optical phonon scattering. At such high electric fields the energy gained by the electrons from the electric field is lost mostly in ionizing collisions that results an electron-hole (e-h) pair. According to Roy and Ghosh, at the ionizing fields the drift velocity v (E) is expressed by

$$v(E) = \frac{v_s}{[(1 + \frac{l_{op}}{l_i})(1 + \frac{\varepsilon_i}{l_i qE})]^{0.5}}$$ (5)

Where lop and li is the mean free path for optical phonon collision and ionizing collision respectively, vs is the saturated drift velocity, ε_i is the threshold energy for ionizing collision , q is the charge of electron and E is the electric field. This theoretical investigation shows that the drift velocity for electrons in Si passes through a maximum before attaining saturation. Danda and Nicolet give an expression which fits well with the experimental results for Si for field dependence of carrier drift velocity in the following form:

$$v(E) = v_s[1 - \exp(-\frac{\mu_o E}{v_s})]$$ (6)

Where v(E) is the carrier drift velocity at field E. The values of low field mobility (μo) of carriers can be obtained from the slopes of v-E curves at low field.

2.2 Impact ionization
At very high electric field (> 10⁷ V.m-1) electrons (minority carriers) gain energy at a faster rate than they can lose through the emission of optical phonon in a reverse biased p-n junction. As

a result, it collides with bound electron in the valence band and excites them into the conduction band, creating an e-h pair and the phenomenon is termed as **impact ionization**. Important parameters for impact ionization are the **ionization threshold energy** E_t (i.e. minimum energy required to cause an ionizing collision) and the **ionization rate** α (i.e. average number of ionizing collisions by the carrier in traversing unit distance in the direction of electric field). From energy conservation principle, E_t should be equal to the band gap energy (E_g). The values of E_g for Si and GaAs at room temperature are 1.10eV and 1.43eV respectively. If both energy and momentum conservation are taken into account, the threshold energy E_t should be equal to $1.5E_g$ for parabolic band structure having the same effective masses for the carrier. If the electron energy exceeds E_t, emission of optical phonons or ionizing collision may produce an e-h pair. The probability of either types of collision depends on the mean free path for optical collision (l_{op}) and on the mean free path for ionizing collision (l_i). The relative probability of second collision being an ionizing collision is $l_{op} l_{i.}$

The ionization rate (α) is a function of l_{op}, l_i, E_t and Eg. In 1954, Wolff first assumed that the probability of ionizing collision is much greater than the optical phonon collision and is valid at high electric field. However, Shockley derive an expression at low field, such that electrons acquire ionization threshold energy E_t and then produces an ionizing collision in the first attempt without suffering a single optical phonon collision which is given by,

$$\alpha = \frac{qE}{r\varepsilon_{op}}\exp(-\frac{E_t}{qEl_r}) \tag{7}$$

The most important theoretical study of field-dependence of ionization rate was carried out by G. A. Baraff, by solving Boltzman transport collision equation in terms of a space and energy dependent collision density, considering the acoustic phonon, optical phonon and ionizing collision. The values of ionization rate 'α' can be obtained from universal Baraffs plot for any semiconductor for which the parameters l_{op}, E_t and ε_{op} are known.

2.3 Avalanche breakdown

Under typical doping profile and reverse bias condition of a p-n junction diode, the total voltage drop occurs across a very thin space charge depletion region. Thermally generated electrons and holes (minority carriers) in the p and n regions diffusing towards the n and p edges of the depletion layer results a small reverse saturation current in the reverse bias condition. A single minority carrier experiences there a very high electric field and creates e-h pair by impact ionization. These generated electron and hole produces additional e-h pair as they further drift toward n and p sides.

If a single electron yield N number of e-h pairs while drifting across the avalanche region of length x_a then,

$$N = \int_{o}^{x_a} \alpha(E)dx \tag{8}$$

Equal ionization rates for electrons and holes generate N^2 number of e-h pairs and the process continues and this is known as avalanche multiplication. Therefore, the total current after avalanche multiplication becomes,

$$J = J_s(1 + N + N^2 + \ldots\ldots\ldots) = \frac{J_s}{1-N} = MJ_s \tag{9}$$

Where J_s is the initial reverse saturation current and M is called the multiplication factor. The current multiplication factors M_n and M_p for electrons and holes are given by J/J_{ns} and J/J_{ps} respectively. A small amount of reverse saturation current (J_{ns}, J_{ps}) multiplied by very high multiplication factor grows to a very high current and this phenomenon is known as avalanche breakdown. At breakdown M and J tends to infinity and then,

$$N = \int_0^{x_a} \alpha(E)dx = 1 \tag{10}$$

Considering the carrier multiplication process initiated by both electrons and holes at the two edges of the depletion layer and unequal ionization rates of charge carriers, Lee et al derived the generalised breakdown condition of the p-n junction. In Fig. 1(a), J_{ps} and J_{ns} are the saturation currents for holes and electrons entering the depletion layer of a reverse biased p-n junction at $x = -x_1$ and $x = x_2$ respectively. The increase of electron and hole current at x is equal to the charges generated per second in distance δx may be written as,

$$\delta J_n = -\delta J_p = \alpha_n J_n \delta x + \alpha_p J_p \delta x \tag{11}$$

Therefore the continuity equations for electrons and holes can be written as,

$$\frac{\partial J_n}{\partial x} = \alpha_n J_n + \alpha_p J_p \tag{12}$$

$$\frac{\partial J_p}{\partial x} = -\alpha_n J_n - \alpha_p J_p \tag{13}$$

Since the diffusion current is very small compared to the drift current, then the hole drift current $J_p = qpv_p$ and the electron drift current $J_n = qnv_n$, where v_p and v_n are the saturated drift velocities for holes and electrons, n and p are the carrier density for electrons and holes. Thus the total drift current density $J = (J_n + J_p)$ is independent of x.

Eliminating J_p from equation (11) one obtains,

$$\frac{\partial J_n}{\partial x} = -(\alpha_n - \alpha_p)J_n = \alpha_n J \tag{14}$$

Using the boundary conditions $J_n(x = 0) = J_{ns}$ and $J_n(x = W) = J - J_{ps}$ and using the integrating factor $\exp\{-\int_0^x (\alpha_n - \alpha_p)dx\}$ the above equation reduces to

$$J_s - J_{ps} + J_{ps}\exp\{-\int_0^W (\alpha_n - \alpha_p)dx\} = J[1 - \int_0^W \alpha_n \exp\{-\int_0^x (\alpha_n - \alpha_p)dx^/\}dx]$$

$$1 - k + k\exp\{-\int_0^W (\alpha_n - \alpha_p)dx\} = M[1 - \int_0^W \alpha_n \exp\{-\int_0^x (\alpha_n - \alpha_p)dx^/\}dx] \tag{15}$$
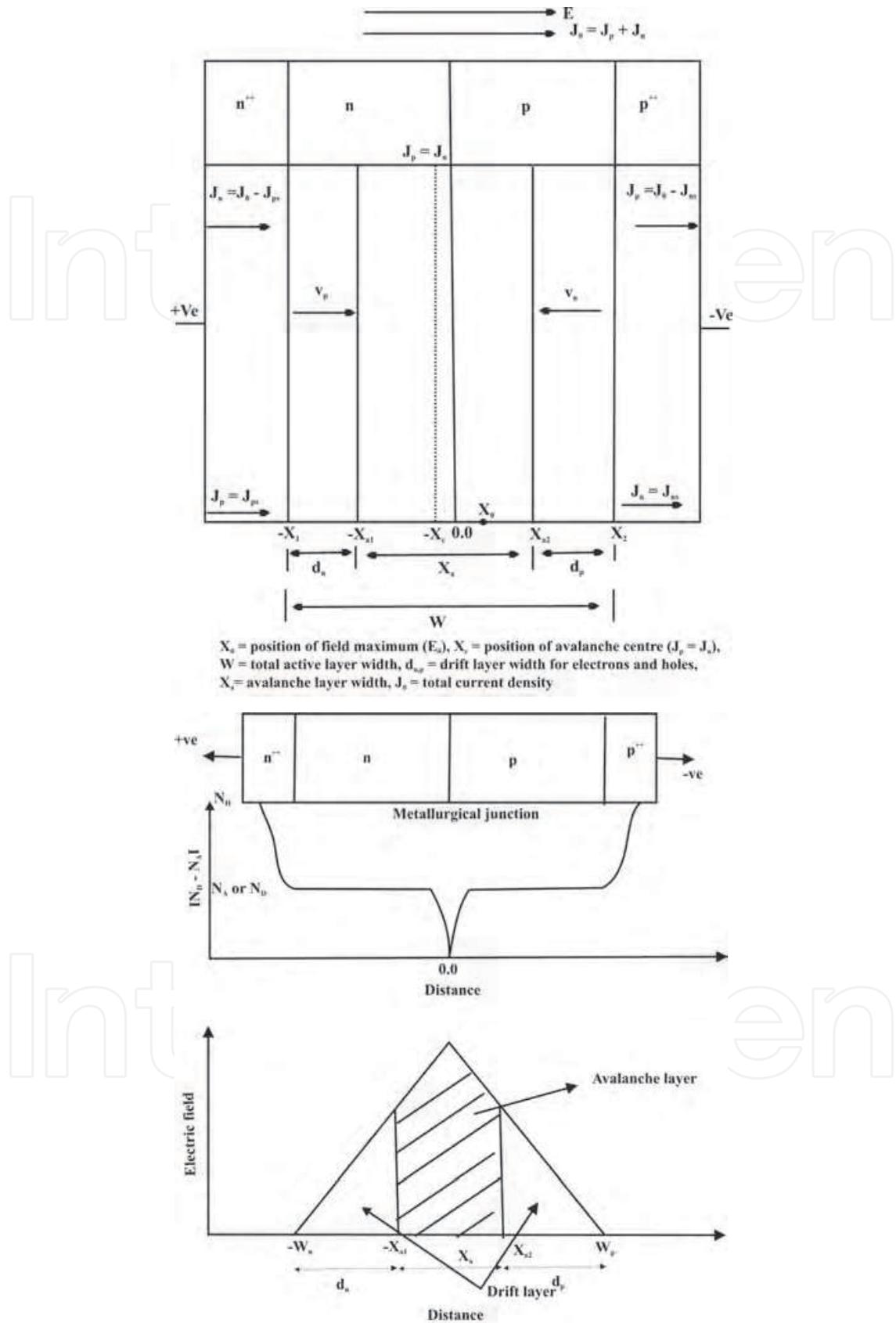
Fig. 1. (a) Avalanche multiplication; (b) carrier current profile and (c) Electric field profile in the depletion region of a reverse biased p-n junction.

Where $\quad k = \dfrac{J_{ps}}{J_s}, \quad M = \dfrac{J}{J_s}$, and $\quad J_n = J_{ns} + J_{ps}$

Where M is the multiplication factor and J_s is the total reverse saturation current. Thus

$$M = [1 - k + k \exp\{-\int_o^W (\alpha_n - \alpha_p)dx\}] / [1 - \int_o^W \alpha_n \exp\{-\int_o^x (\alpha_n - \alpha_p)dx^/\}dx]$$

$$\frac{1}{M} = \frac{1}{\xi}[1 - \int_o^W \alpha_n \exp\{-\int_o^x (\alpha_n - \alpha_p)dx^/\}dx] \qquad (2.4.8)$$

Where $\quad \xi = 1 - k + k \exp\{-\int_o^W (\alpha_n - \alpha_p)dx\}$

In a similar way using the boundary condition, $J_p(x = o) = J - J_{ns}$ and $J_p(x = W) = J_{ps}$ we get,

$$\frac{1}{M} = \frac{\exp\{-\int_o^W (\alpha_n - \alpha_p)dx\}}{\xi}[1 - \int_o^W \alpha_p \exp\{\int_o^x (\alpha_n - \alpha_p)dx^/\}dx] \qquad (16)$$

Multiplying equation (15) by (1-k) and equation (16) by k and adding one obtain,

$$1 - \frac{1}{M} = \frac{1-k}{\xi}\int_o^W \alpha_n \exp\{-\int_o^x (\alpha_n - \alpha_p)dx^/\}dx +$$

$$\frac{k}{\xi}\exp\{-\int_o^W (\alpha_n - \alpha_p)dx\}.\int_o^W \alpha_p \exp\{\int_o^x (\alpha_n - \alpha_p)dx^/\}dx \qquad (17)$$

Now, M may be written as,

$2M = (1-k)M_n + kM_p$ where $\quad M_n = \dfrac{J}{J_{ns}}$ and $\quad M_p = \dfrac{J}{J_{ps}}$

When avalanche breakdown occurs i.e. M tends to infinity for a mixture of electron and hole injection, one obtain,

$$\frac{1-k}{\xi}\int_o^W \alpha_n \exp\{-\int_o^x (\alpha_n - \alpha_p)dx^/\}dx +$$

$$\frac{k}{\xi}\exp\{\int_o^W (\alpha_n - \alpha_p)dx\}.\int_o^W \alpha_p \exp\{-\int_o^x (\alpha_n - \alpha_p)dx^/\}dx = 1 \qquad (18)$$

In case of pure electron or hole injection i.e. in which multiplication is initiated purely by electrons $(k = 0, J_{ps} = 0)$ or purely by holes $(k = 0, J_{ns} = 0)$, the breakdown condition reduces to

$$1 - \frac{1}{M_n} = \int_o^W \alpha_n \exp\{-\int_o^x (\alpha_n - \alpha_p) dx^/ \} dx = 1 \qquad (2.4.12a)$$

$$1 - \frac{1}{M_p} = \int_o^W \alpha_p \exp\{\int_o^x (\alpha_n - \alpha_p) dx^/ \} dx = 1 \qquad (19)$$

For $\alpha_n = \alpha_p$, the above equation reduces to $N = \int_o^{x_a} \alpha(E) dx = 1$.

Therefore, the above equation governs the avalanche breakdown, the static and dynamic properties of IMPATT diodes. The enhancement of mobile space charge density modify the electric field profile, breakdown voltage and the depletion layer width, because the ionization rates get modified at various points in the space charge layer.

2.4 Basic IMPATT phenomena

The operation of an IMPATT device is based on two basic physical mechanisms: one is the **avalanche multiplication** caused by **impact ionization** [4] and the other is the **finite transit time** required by the charge carriers to **cross the depletion layer** with saturated drift velocity. The avalanche process turns out to be an inductive process causing a phase delay between the applied r.f. voltage and the generated r.f. current. The transit-time process adds an extra phase delay. Thus the device exhibits a high-frequency negative resistance when the combined phase delay due to the avalanche process and the finite transit time of the drifting carriers lie between 90^0 and 270^0.

The IMPATT phenomena were studied by Read and Misawa by considering two different devices models. Read considered an n⁺-p-i-p⁺ diode structure and assumed that the spatial extent of avalanche zone is negligibly small. But Misawa in his p-i-n avalanche diode structure assumed an extended avalanche zone. However, in practical IMPATT structure like SDR, DDR etc, the avalanche zone is neither too thin like Read diode nor too wide like Misawa diode but it is intermediate between the two having finite avalanche zone width. In section 2.5.1 mechanisms of IMPATT mode of operation has been discussed with reference to (a) Read and (b) Misawa diodes and in the nest section and a brief overview of various practical IMPATT diode structures will be presented.

Several authors including Read and Misawa have carried out analysis of microwave/mm-wave properties for different IMPATT structures and have found that the active diode impedance when the device generates microwave/mm-wave can be represented by a high frequency negative resistance in series with a capacitance .The magnitude of the negative resistance being much smaller than the capacitive impedance, the device is mainly capacitive.

2.5 Mechanism of IMPATT mode of operation in (i) read diode and (ii) misawa diode
2.5.1 Read diode

A schematic diagram of Read diode structure n⁺-p-i-p⁺ along with its doping profile and electric field distribution at reverse biased to avalanche breakdown is shown in Fig. 2. In the Read structure the superscript plus sign denotes very high doping and the i or ν refers to

intrinsic material .The device consists essentially of two regions ; One is the narrow p-region at which avalanche multiplication occurs .This region is also called the **high field region or the avalanche region** .The other is the i (or ν) region through which the generated holes must drift while moving towards the p$^+$ contact .This region is also called the **intrinsic region or the drift region** .When the reverse biased voltage is well above the punch through or breakdown voltage, the space between the n$^+$p junction and the i-p$^+$ junction happens to be the space-charge region . Carriers (holes) moving in the high field near the n$^+$-p junction acquire energy to knock valance electrons into the conduction band, thus producing hole-electron pairs. The rate of pair production, or avalanche multiplication, is a sensitive nonlinear function of the field. By proper doping, the field can be given a relatively sharp peak so that avalanche multiplication is confined to a very narrow region at the n$^+$-p junction. The electrons move in to the n$^+$- region and the holes drift through the space charge region to the p$^+$- region with a constant velocity v_d (called the saturated drift velocity).The transit time of a hole across the drift region (i.e. i-region of length L) is given by τ = L/ v_d.

The phenomenon of negative resistance in Read diode can be understood with reference to Fig. 3. In actual practice, to form oscillator, the diode is mounted in a microwave/mm-wave resonant circuit. An a.c. voltage can be maintained at a given frequency in the circuit thus the total voltage across the diode is the sum of the d.c. and a.c. voltages, mathematically : V_T (t)=V_{DC} + V_D sin ωt , and the form of this total diode voltage is shown in Fig. 3(a). This total voltage causes breakdown at the n$^+$ - p junction during the positive half cycle of the a.c. voltage when V_T is above the breakdown value, and the carrier current (i.e. the hole current in this case) I_o(t) generated at the n$^+$ p junction by the avalanche multiplication grows exponentially with time while the voltage is above the critical (i.e. breakdown) value. During the negative half cycle, when V_T is below the breakdown voltage for the diode, the current I_o(t) decays exponentially to a small steady state value. The carrier current I_0(t) is the current at the junction only and is in the form of a pulse of very short duration as shown in Fig. 3(b). Therefore, the carrier current I_0(t) reaches its maximum in the middle of the a.c. voltage or lags by 90^0 behind the said a.c. voltage. The direction of the electric field is such that the generated holes are injected into the space-charge region towards the negative terminal. An equal number of generated electrons move to the left, back into the n$^+$ - contact to maintain space charge neutrality .As the injected holes traverse the drift space, they induce a current I_e (t) in the external circuit which is approximately a square wave as shown in fig.3(c).The current I_e (t) flows in the external circuit for a time τ during which the holes are moving across the space-charge region. Thus, on the average, the external current I_e (t) due to the moving holes is delayed by τ/2 or 90^0 relative to the pulsed carrier current I_0 (t) generated at the n$^+$-p junction .Because the carrier current I_0 (t) is already delayed by 90^0 relative to the a.c. voltage, the external current I_e (t) is then delayed by as a total of 180^0 relative to the applied a.c. voltage .In general, a device exhibits negative resistance at its terminals when the a.c. current flowing though it lags the a.c. voltage by a phase angle which lies between 90^0 and 270^0 .

2.5.2 Misawa diode

The device structure, doping profile and electric field distribution of Misawa diode i.e. a p-i-n diode reverse biased to avalanche breakdown is shown in Fig. 4 (a-c). Misawa assumed an

(a)

(b)

(c)
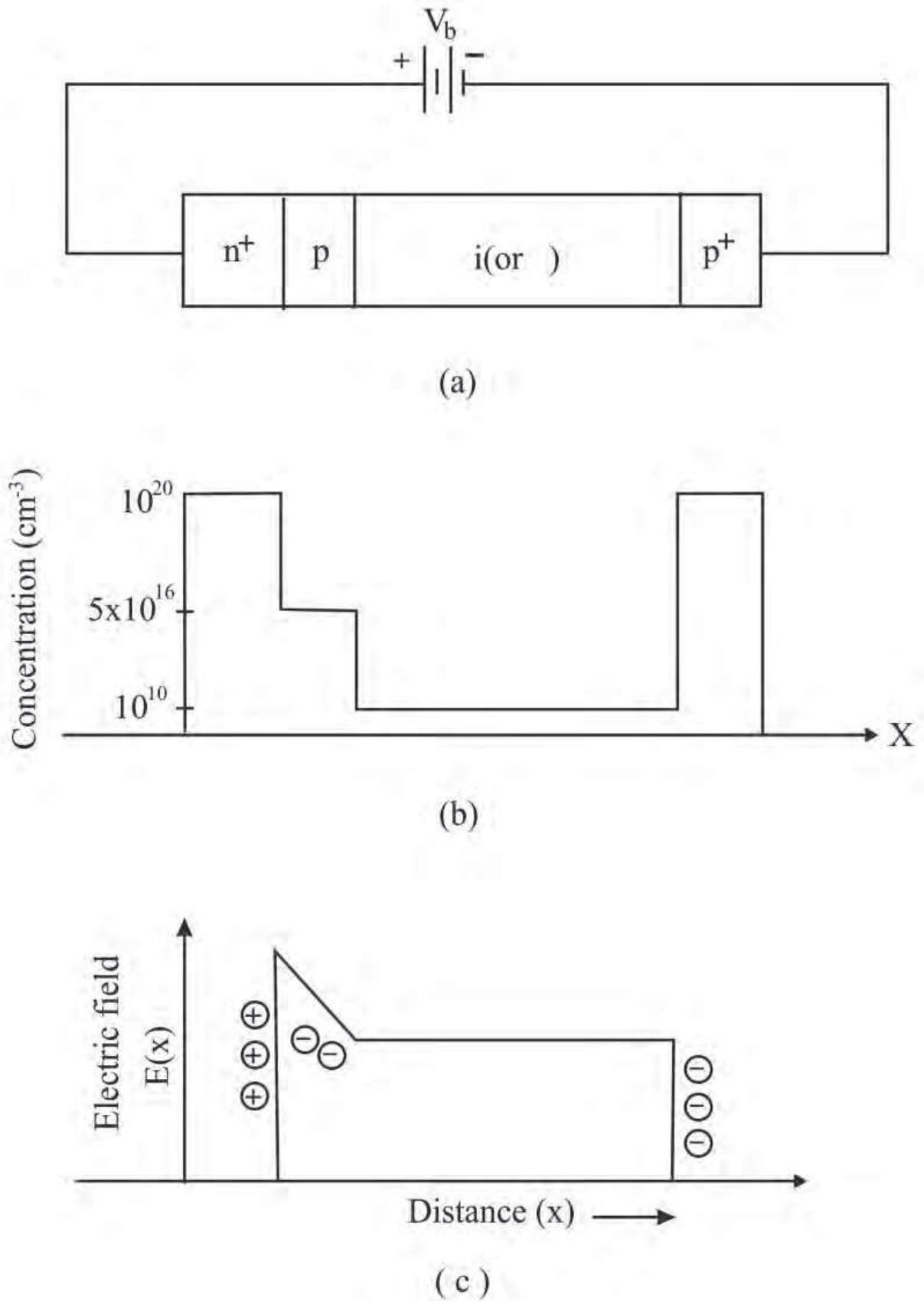
Fig. 2. (a) Read (n⁺-p-i-p⁺) structure (b) Doping profile and (c) Electric field distribution.
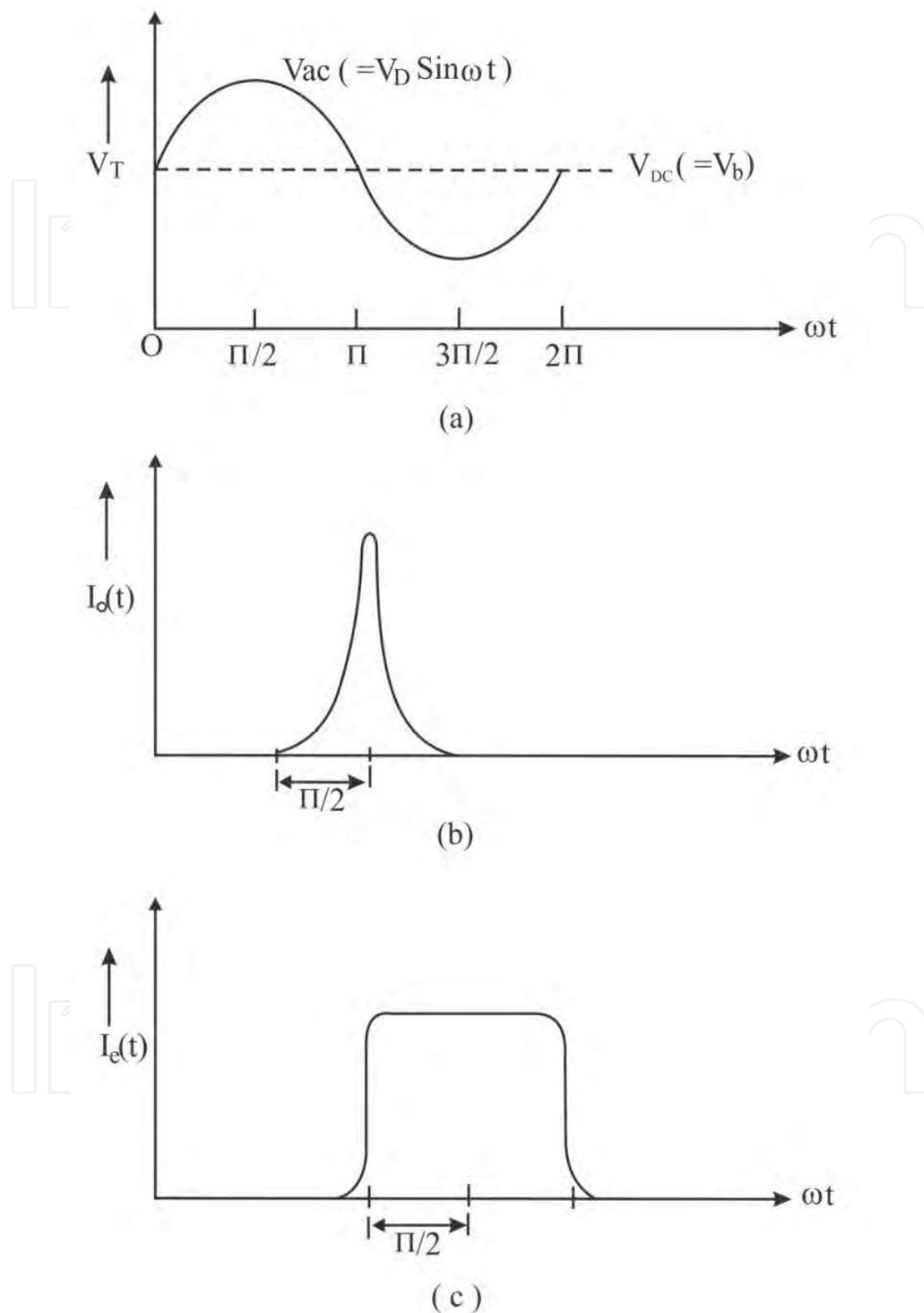
Fig. 3. Voltage and currents in Read diode, (a) Total diode voltage, (b) Carrier current generated at n⁺-p junction by avalanche multiplication and (c) Current induced in the external circuit.

uniform avalanching i.e. the field remains high enough for avalanche multiplication of charge carriers to take place throughout the active region (i.e. i-region). The origin of negative resistance can be understood as follows. The electrons and holes enter the i-region from the p- and n- regions respectively Fig. 4 (a) and they move with saturated velocities and generates holes and electrons simultaneously in this region. Now let us consider a fluctuation in the electron density ($\tilde{n}_0$) in the i-region which will be moving towards the x-direction with saturated drift velocity being carried by the electrons moving is the same direction Fig. 4(d) .The electric field wave ($\tilde{E}$) caused by this perturbation in the electron density lags the electron density wave by 90^0. Now the generation rate of electron-hole pairs is larger both when the electric field is stronger and when there are more carriers. Therefore, in this case of an electron density perturbation the generation rate peaks somewhere between the place where the field is strongest and the place where the density is largest. This means that the generation rate (G) leads the electron density wave by less than 90^0 .It is to be noted that since the d.c. field is in negative x-direction, the field becomes strongest at its negative peak. The increased generation rate gives rise to an excess electron density ($\Delta\tilde{n}$) which lags the rate by 90^0. Thus the resultant electron density ($\tilde{n}$) gives a current ($\tilde{j}_n$) which lags the field by more than 90^0 .The current due to hole density wave also lags the field by more than 90^0 .The situation is shown in Fig. 4 (e) .Thus the current generated in the device lags the field by more than 90^0 and hence the device exhibits negative resistance property.

2.6 Practical IMPATT diode

The Read and Misawa diodes that have been discussed are idealized IMPATT structures. But practical IMPATT diodes which have been fabricated and are in wide use are intermediate between the two in the sense that the avalanche zone is well defined having a finite width neither too thin nor too wide. The charge is injected from a well defined avalanche zone into the drift zone approximately 90^0 behind the r.f. voltage and then the injected charge travels with saturated drift velocity in the drift region. The practical Single Drift Region (SDR) and Double Drift Region (DDR) IMPATT which are now commonly used belong to this category. Diodes have been fabricated from various semiconductor materials i.e. Germanium, Silicon, Gallium Arsenide, Indium Phosphide and recently from Silicon Carbide.

2.7 Impedance properties and equivalent circuit of IMPATT diode

A knowledge of the nature of device impedance is quite important to understand the mechanism of microwave/mm-waves generation by IMPATT diodes. Also an insight into the impedance properties of the device helps one to choose the microwave/mm-wave circuit necessary to construct oscillators with these devices. Several authors including Read , Gilden and Hines have analyzed the small-signal impedance properties of Read type IMPATT diode. Misawa has calculated the small signal impedance of the p-i-n avalanche diode both analytically and numerically. Gummel and Scharfetter extended the small signal analysis of Gilden and Hines and obtained small-signal admittance plots for a more realistic Read structure. Also Scharfetter and Gummel carried out large-signal numerical solution for Si Read diode and obtained the diode admittance as a function of frequency and r.f. voltage amplitude.
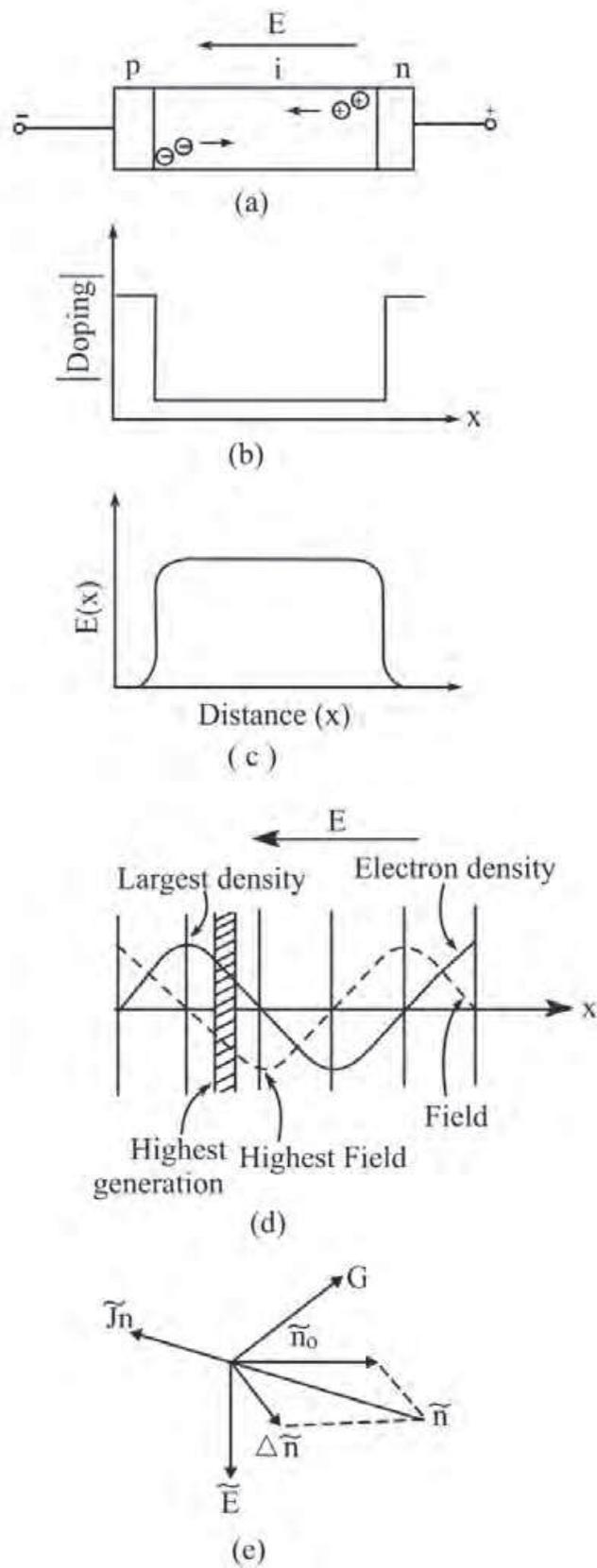
Fig. 4. (a) Misawa diode (p-i-n) structure, (b) Doping profile (c) Electric Field distribution (d) Electric field and generated electron density wave and (e) Phase diagram (current and field)

Gilden and Hines derived an expression for the diode terminal impedance in a Read type structure by assuming a thin avalanche zone where space charge and signal delay is negligible and a wide drift zone where no carriers are formed but where space-charge and transit time effects are significant. Denoting Z_a as avalanche zone impedance, Z_d as drift zone impedance and R_s as the passive resistance of the inactive zone , Gilden and Hines obtained the following expression for the terminal impedance

$$Z = R_s + Z_a + Z_d = R_s + \frac{1}{j\omega C_a}\left(1 - \frac{\omega_a^2}{\omega^2}\right)^{-1} + \frac{1}{\omega C_d}\left\{\left(1 - \frac{\omega^2}{\omega_a^2}\right)^{-1}\left(\frac{1 - Cos\theta}{\theta}\right)\right\} +$$

$$+ \frac{1}{j\omega C_d}\left\{1 - \left(1 - \frac{\omega^2}{\omega_a^2}\right)^{-1}\left(\frac{Sin\theta}{\theta}\right)\right\} \tag{20}$$

where ,

$C_a = \dfrac{\in A}{l_a}$, avalanche zone capacitance

$C_d = \dfrac{\in A}{l_d}$, drift zone capacitance

$\theta = \dfrac{\omega l_d}{v_d}$, transit angle in the drift zone

$\omega_a^2 = \dfrac{2\alpha' v_d J_0}{\in}$, avalanche resonance frequency

with $\alpha' = \dfrac{d(\alpha)}{dE}$, the derivative of ionization rate w.r.t. electronic field E , J_0 is the d.c. current density . l_a and l_d the avalanche zone and drift zone lengths, v_d is the saturated drift velocity , A is the cross - sectional area , and $\in$ is the permittivity .

It can be observed from equation (20) that the avalanche zone is represented by an antiresonant circuit as shown in Fig. 5 .The drift zone consists of a resistive and a reactive part .The resistive part (i.e. the real part of Z_d) is negative for all frequencies above ω_a (except for nulls at $\theta = 2\pi$ x integer) and below this frequency it is positive .It is important to note that the avalanche zone does not contribute to the device negative resistance. For small transit angles i.e. for $\theta < \pi/4$, equation (20) reduces to :-

$$Z = R_s + \frac{l_d}{v_d \in A}\left(1 - \frac{\omega^2}{\omega_a^2}\right)^{-1} + \frac{1}{j\omega C}\left(1 - \frac{\omega^2}{\omega_a^2}\right)^{-1} \tag{21}$$

Where , $C = \dfrac{\in A}{l_a + l_d}$.

A typical plot of equation (21) is shown in Fig.6. It is observed that the diode reactance, X , changes from inductive to capacitive at the avalanche resonance frequency and also the resistive part , R, changes sign at the same frequency and become negative above ω_a .Thus the device possesses negative resistance for all frequencies above ω_a and there the device reactance is capacitive.
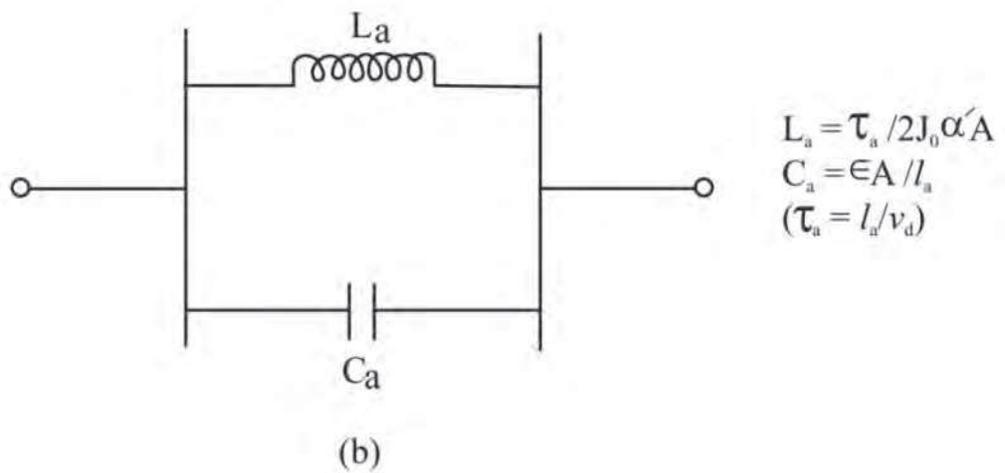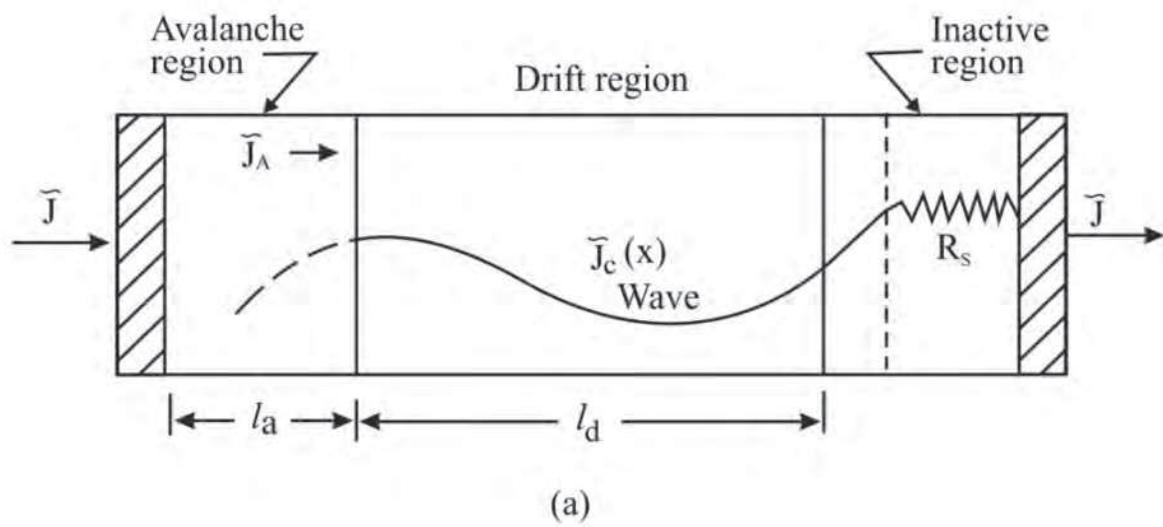
Fig. 5. (a) Model of Read diode with avalanche region, drift region and inactive region. (b) Equivalent circuit of the avalanche region.
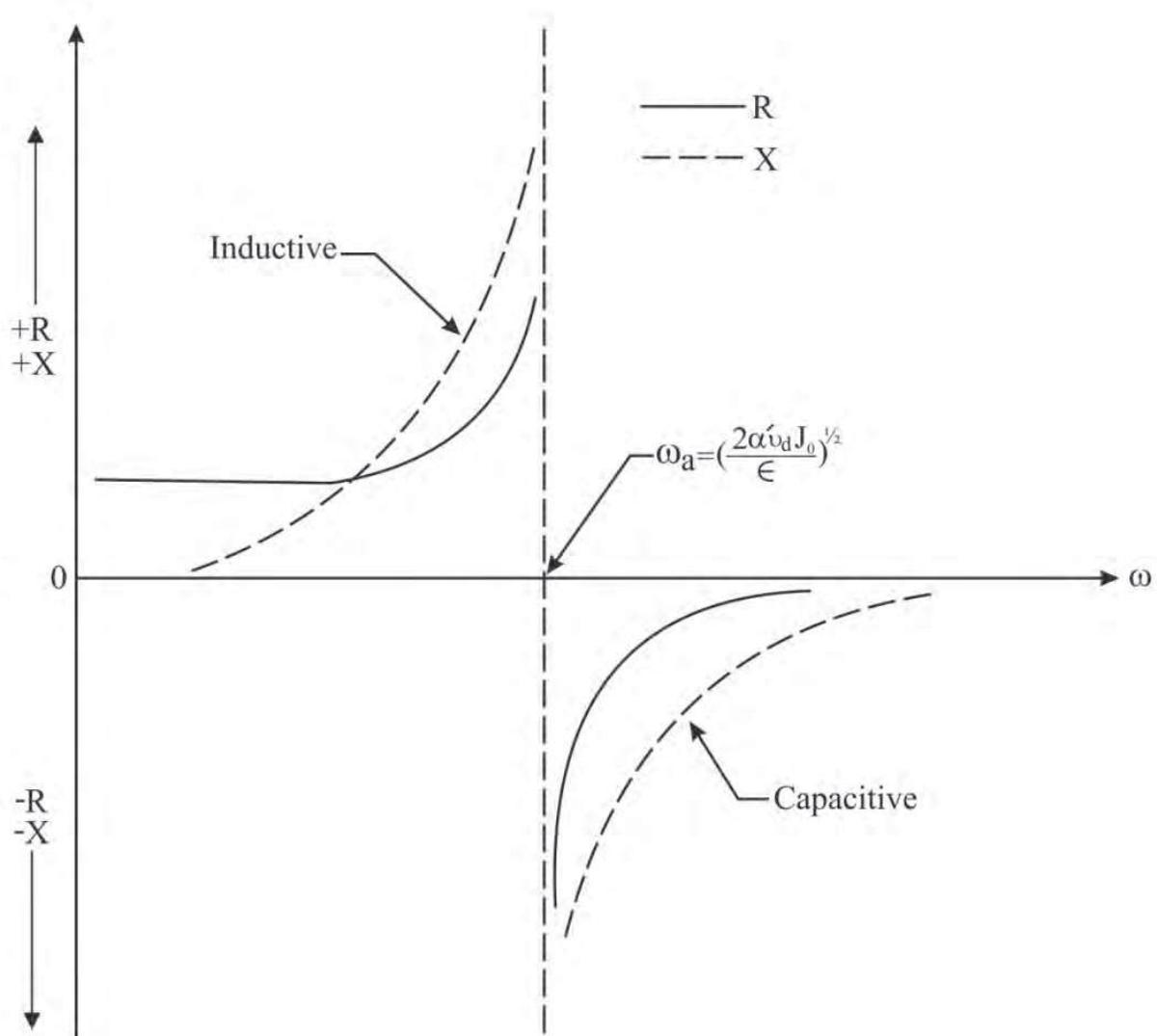
Fig. 6. Typical Impedance variation with frequency for a Read diode.

Gummel and Scharfetter extended the small-signal analysis of Gilden and Hines to include diode in which the avalanche region is not necessarily narrow .They obtained small signal admittance plots for a Read diode and for more realistic diode structures in which the avalanche region occupies an appreciable fraction of the total depletion region. They found that the optimum performance is achieved when the avalanche region is one third of the drift region. Scharfetter and Gummel have developed large-signal numerical analysis for Read diodes with a realistic doping profile including the effect of microwave circuit in which the diode is placed.

The results of investigation on impedance properties of IMPATT diode by various workers can be summed up to obtain an idea of the r.f. equivalent circuit for the IMPATT diode chip. In general, the diode equivalent circuit will consist of a negative resistance $-R_D$ in series with a capacitive impedance X_D (or alternatively by a negative conductance $-G_D$ in parallel with a capacitive susceptance B_D). The r.f. equivalent circuit of IMPATT diode chip is shown in Fig. 7 (a). Some important observation regarding the nature and values of R_D and X_D is worth mentioning. First, the magnitude of R_D is usually much smaller than X_D. Consequently, the magnitude of the chip impedance is approximately equal to X_D. Secondly, for most cases of

interest, X_D can be approximated with sufficient accuracy by the reactance of the junction (chip) capacitance at the breakdown voltage. Thirdly, the values of the negative resistance are generally small compared with the usual transmission line impedances. Further, it may be mentioned that the magnitude of negative resistance of IMPATT diode varies with signal level and that it increases with increasing signal level.

The properties of IMPATT diode chip have so far been discussed, but the chip by itself is difficult to handle and it is prone to mechanical damage and environmental contamination. So, it is necessary to provide the diode chip with a robust, hermetically sealed package. The package also provides the necessary heat- sink arrangements for dissipating the heat from the diode chip to the ambient .A common type of commercially available S4 package has been shown in Fig.2.6.3.(b) and also equivalent circuit of the packaged IMPATT diode having packaged parasitics . To a good approximation, the package can be described by two reactive elements a series inductance, L_p and a shunt capacitance C_p .The exact values of L_p and C_p varies from one package style to another.
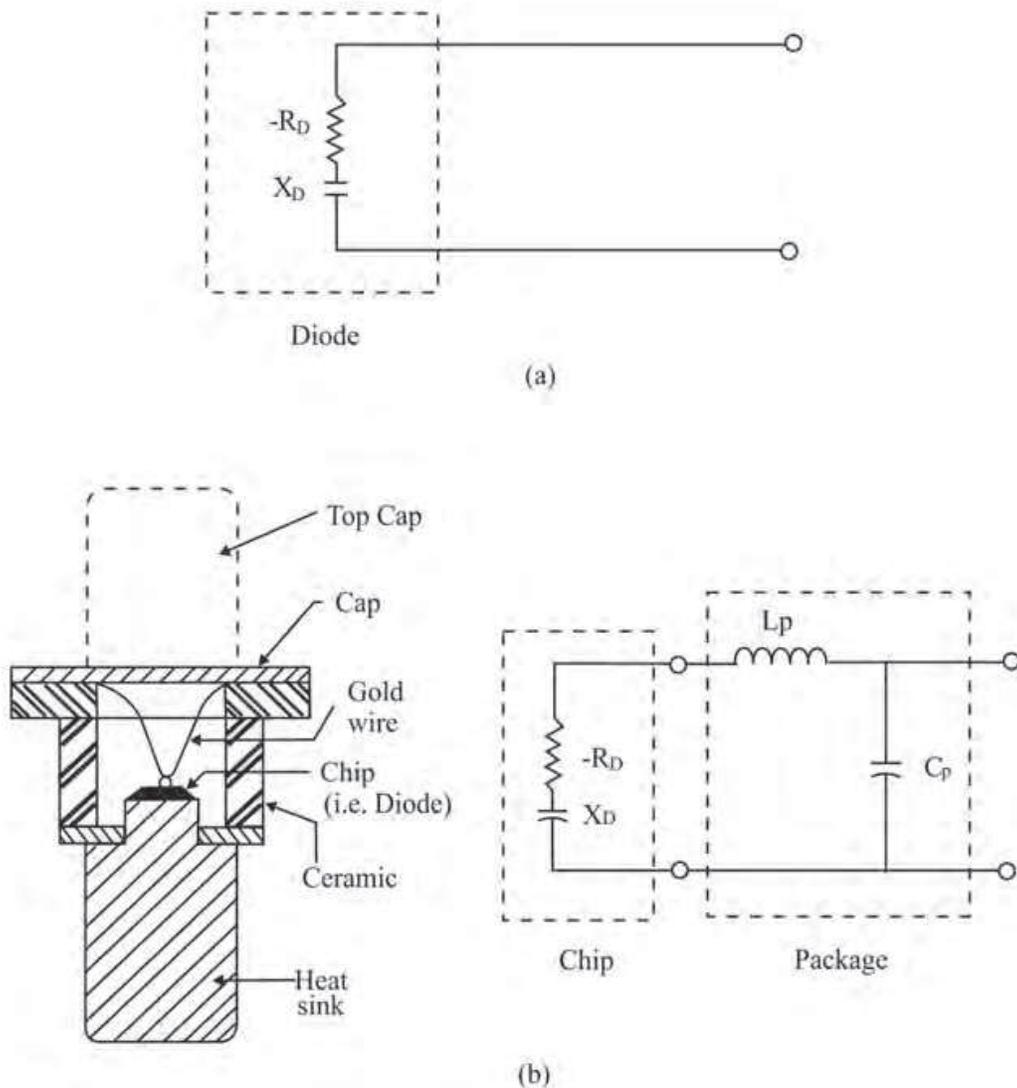
Fig. 7. (a) IMPATT diode chip r.f. equivalent circuit and (b) Cross-section of the chip in S4 package with equivalent circuit of the packaged IMPATT diode.

3. Simulation experiment

Different polytypes of SiC are shown in Figure 8. At first, SiC diodes are designed and optimized through a generalized double iterative simulation technique used for the analysis of IMPATT action [1]. The fundamental device equations, i.e. the one-dimensional *Poisson's* equation and the combined current continuity equations under steady-state conditions, have been numerically solved subject to appropriate boundary conditions, through an accurate and generalized double iterative computer algorithm, described elsewhere. Iteration over the value and location of field maximum are carried out until the boundary conditions of $E(x)$ and $P(x) = [J_P(x) - J_n(x)]/J_0$ are satisfied at both the edges of diode active layer. The DC solution gives the electric field $E(x)$ profile, normalized current density $P(x)$ profile, the maximum electric field (E_m), drift voltage drop (V_D), breakdown voltage (V_B) and avalanche zone width (x_a). The breakdown voltage (V_B) is calculated by integrating the spatial field profile over the total depletion layer width. The boundary conditions for current density profiles are fixed by assuming a high multiplication factor ($M_{n, p}$) ~ 10^6, since it is well known that, avalanche breakdown occurs in the diode junction when the electric field is large enough such that the charge multiplication factors (M_n, M_p) become infinite. The edges of the depletion layer are also determined accurately from the DC analysis.

The small-signal analysis of the IMPATT diode provides insight into the high-frequency performance of the diode. The range of frequencies exhibiting negative conductance of the diode can easily be computed by *Gummel-Blue* method [2]. From the DC field and current profiles, the spatially dependent ionization rates that appear in the *Gummel-Blue* equations are evaluated and fed as input data for the small-signal analysis. The edges of the depletion layer of the diode, which are fixed by the DC analysis, are taken as the starting and end points for the small-signal analysis. The spatial variation of high-frequency negative resistivity and reactivity in the depletion layer of the diode are obtained under small-signal conditions by solving two second order differential equations in $R(x, \omega)$ and $X(x, \omega)$. $R(x, \omega)$ and $X(x, \omega)$ are the real and imaginary part of diode impedance $Z(x,\omega)$, such that, $Z(x,\omega) = R(x, \omega) + j X(x, \omega)$. The total integrated diode negative resistance (Z_R) and reactance (Z_x) at a particular frequency (ω) and current density J_0, are computed from numerical integration of the $R(x)$ and $X(x)$ profiles over the active space-charge layer.

At resonance, the reactance of the resonant cavity is mainly capacitive in nature. When the magnitude of negative conductance of the diode $|-G|$ is equal to the load conductance G_L, the condition of resonance is satisfied and as a result, power is absorbed in G_L and at the same time oscillation starts to build up in the circuit. *Adlerstein et al.* developed a method for determining R_S from the threshold condition of IMPATT oscillation [3]. In the present method, the author has determined the value of series resistance (R_S) from the admittance characteristics using a realistic analysis of *Gummel-Blue* [2] and *Adlerstein et al* [3]. The author has considered the effect of R_S in the realistic analysis of output power from the THz diodes.

The basic mechanism of optical control of IMPATT diode is discussed earlier. In summary, the leakage current entering the depletion region of the reversed biased p-n junction of an un-illuminated IMPATT diode is only due to thermally generated electron-hole pairs and it is so small that the multiplication factors ($M_{n, p}$) become very high. When optical radiation of suitable wavelength (photon energy $hc/\lambda > E_g$) is incident on the active layer of the device, the leakage current increases significantly due to photo-generation of charge carriers. The enhancement of the leakage current under optical illumination of the devices is manifested as the lowering of $M_{n,p}$. The photo-sensitivity of IMPATTs are studied under two

illumination configuration: (a) Top Mounted and (b) Flip chip. The corresponding diagrams are shown in Figure 9.

In order to assess the role of leakage currents in controlling the dynamic properties of IMPATT oscillators at THz frequencies, simulation experiments are carried out on the effect of electron current multiplication factor, M_n, (keeping hole current multiplication factor M_p very high ~ 10^6) and M_p (keeping M_n very high ~ 10^6) on (i) the small-signal admittance characteristics, (ii) the negative resistivity profiles, (iii) quality factor at peak frequencies (Q_p), (iv) device negative resistance at peak frequencies ($-Z_{RP}$) and (v) maximum power output of DDR SiC IMPATTs.

4. Observations from simulation experiment

DC simulation program is used to obtain the $E(x)$ and $P(x)$ profiles of flat profile SiC IMPATT diodes which are designed and optimized for operation at 0.3 THz regime. The optimized design parameters and corresponding bias current densities for each diode are shown in Table 1. In figures 10(a-c), plots of $E(x)$ and $P(x)$ profiles of DDR SiC based un-illuminated and illuminated (TM and FC configuration) IMPATTs are presented. It is intersting to note that there are small changes in the electric field profile due to the lowering of Mn, corresponding to TM illumination configuration, while the variation is comparatively much prominent due to the lowering of MP, corrsponding to FC illumination configuration. Analysis of $P(x)$ profiles, as shown in figure 10(a-c), reveals that avalanche centre, at which JP =Jn, moves towards the metallurgical junction from n-side with the lowering of both Mn and Mp. Similar to $E(x)$ profiles, $P(x)$ profiles of SiC based DDRs are also much sensitive to hole leakage current. Table 2 shows that the 4H-SiC IMPATT breaks down at 135.0 V , which is atleast 22.7% higher than its 6H-SiC and 3C-SiC counterpart. The variation of breakdown voltage (VB) of the designed SiC based IMPATTs, with the enhancement of photo-leakage current is shown in Figure 11. It is clear that compare to TM illumination configuration, in case of FC illumination

configuration the diode breakdown voltages decreases more. Moreover, the breakdown voltage of the illuminated hexagonal SiC based devices reduces much than its illuminated cubic SiC counterpart.

DDR diode type	Doping conc. (n region) (10^{23} m^{-3})	Doping conc. (p region) (10^{23} m^{-3})	Width of the n region (nm)	Width of the p region (nm)	Current density (10^9 A m^{-2})
4H-SiC	6.5	6.5	250.0	250.0	3.4
6H-SiC	8.0	8.0	250.0	250.0	3.5
3C-SiC	8.0	8.0	250.0	250.0	3.7

Table 1. Design Parameters of SiC IMPATT Diodes at 0.3THz Frequency

4H-SiC based diode is found to be more efficient (14%) than 6H-SiC and 3C-SiC based diodes, under almost similar operating condition. Moreover the negative conductance of the 4H-SiC IMPATT is found to be ~ 55.0% and 7.0% higher than 6H-SiC and 3C-SiC based IMPATT. The higher value of diode breadown voltage and negative conductance in 4H-SiC based diode icreases the RF power level. It is clear from the table 2, that 4H-SiC based

IMPATT is capable of delivering a RF power density of 36.45×10^{10} Wm^{-2} , which is ~2.5 times and 1.6 times higher than 6H-SiC and 3C-SiC based IMPATTs, respectively. Furthermore, the device negative resistance (-Z_{RP}) at peak frequencies of the 4H-SiC based device is atleast 45% higher than its counterparts. The higher value of negative resistance is an essential criterian for getting sustained oscillation from the THz devices. The quality factor of 4H-SiC based device is found to be best among all the designed diodes.

Diode parameters	4H-SiC DDR	6H-SiC DDR	3C-SiC DDR
Peak electric field (E_m) (10^8 V m^{-1})	4.25	3.8	5.65
Breakdown voltage (V_B) (V)	135.0	109.0	110.0
Efficiency (η) (%)	14.0	12.0	12.5
Peak frequency (f_p) (THz)	0.325	0.35	0.353
Peak negative conductance (-G_p) (10^6 S m^{-2})	162.0	102.0	152.0
Device quality factor (-Q_p)	1.26	2.45	1.79
Device negative resistance at peak frequency (-Z_{RP}) ($10^{-9}\Omega m^2$)	2.35	1.30	1.60
RF output power density (P_{RF}) (10^{10} Wm^{-2})	36.45	15.15	22.99

Table 2. DC and high-frequency properties of SiC IMPATT Diodes at around 0.3 THz Frequency

The values of RS for all the three designed diodes are estimated from Adlerstein's approach, as mentioned in earlier section and the results are shown in Table 3. It is depicted that among all the designed diodes, the magnitude of parasitic positive series resistance is least in case of 4H-SiC based devices. Moreover, Table 3 also shows that the ratioes of negative resistance : positive series resistance in 4H-SiC , 6H-SiC and 3C-SiC based diodes are 3.3: 2.21: 2.96. The much higher value of negative resistance than its positive series resistance in 4H-SiC based device indicates that IMPATT diode based on 4H-SiC material system will be an potential candidate for generating THz power. The effects of RS on the admittance characteristics of the devices are shown in Fgure 12. Figure 12 indicates that parasitic series resistance degrades the admittance charecteristics of the designed SiC based DDRs. The degradation of admittance charecteristics due to the presence of RS is more serious in 6H-SiC based IMPATT.

Thus the present study definitely establishes that the prospects of 4H-SiC based IMPATT as a high power, efficient THz source is far better than its 6H-SiC and 3C-SiC counterparts.

The effects of optical illumination on the THz behavior of the designed diodes are shown in Table 4. The computed values of –GP, -ZRP, PRF, fP and –QP for different electron and hole current multiplication factors are shown in Table 4. Admittance plots of all the SiC DDR IMPATTs under optical illumination are shown in Figure 13. It is evident from the Figure as well as from Table 4 that the values of │-GP│ at the optimum frequencies decrease with the lowering of Mn and Mp. At the same time, the frequency ranges over which the devices exhibit negative conductance, shift towards higher frequencies with the

lowering of Mn and Mp. The simulated results for the illuminated 4H-SiC IMPATT diode (Table 4) indicate that the values of │-GP│and PRF decrease nearly by the same percentage (~3.8.0 %) as Mn decreases from 106 to 25, keeping the value of MP constant at 106. On the other hand, for a similar variation of Mp from 106 to 10 (keeping the value of Mn constant at 106), reduces the values of │-GP│ and PRF by ~ 35.0 %. Similar trend is reflected in Figure 13. In the case of 6H-SiC and 3C-SiC IMPATT diodes, as the value of Mn decreases from 106 to 25 (corresponding to TM illumination configuration), │-GP│ and PRF decrease by 5.2 % and 2% , respectively (Table 4). Similarly for the FC illumination configuration of 6H-SiC and 3C-SiC IMPATTs, the decrease of MP from 106 to 25, causes a reduction in the values of │-GP│ and PRF by 18.2% and 21.6 %, respectively.

Diode type	Negative conductance (-G) (10^6 Sm^{-2})	Susceptance (B) (10^6 Sm^{-2})	Estimated load conductance (g) (10^6Sm^{-2})	Negative resistance ($-Z_R$) ($10^{-9}\Omega$m^2)	Series Resistance (R_S) (10^{-9} Ωm^2)
4H-SiC	153.0	150.0	130.0	3.34	1.02
6H-SiC	95.0	152.0	63.7	2.95	1.33
3C-SiC	150.0	153.0	125.0	3.26	1.1

Table 3. Series resistance of the designed diodes at THz regime (frequency = 0.3 THz)

It is evident from Table 4, that in the case of 4H-SiC based TM diode, a lowering of Mn from 106 to 25 causes the diode negative resistance (-ZRp) to decrease by 3.0%, while there is a corresponding lowering of -ZRp by 51.0 % in case of FC diode. Similarly for TM 6H-SiC and 3C-SiC diodes, the value of -ZRp reduces by 20.0% and 10.0 %, respectively, as Mn decreases from 106 to 25 (Table 4), whereas, for a similar variation of MP, │-ZRp│ reduces by 40.0 % and 25.0 % , respectively in 6H-SiC and 3C-SiC based diodes. The device quality factors are also found to degrade with the lowering of Mn and MP, in case of all the SiC based diodes.

It is further evident from figure 13 that in α-SiC and β-SiC based DDR devices a lowering of Mp causes larger upward shift in frequency than corresponding lowering of Mn. The optimum frequency of oscillation (fP) shifts upwards by 15.0 GHz and 45.0GHz respectively for TM and FC IMPATTs based on 4H-SiC. On the other hand, in case of 6H-SiC and 3C-SiC based TM IMPATTs, fP shifts upward by 1.0 GHz and 2.0 GHz, respectively. Whereas under FC illumination configuration, the values of fP shifts upward by 3.0 GHz and 7.0 GHz respectively for 6H-SiC and 3C-SiC based diodes.

Thus the studies reveal that, effects of photo-illumination on the frequency up shift as well as on the modulation of the THz behavior of the SiC devices are found to be more pronounced in FC illumination configuration than that for TM illumination configuration under similar operating condition. These results show an identical trend as observed previously for MM-wave SiC devices [4].

DDR diode type	M_n	M_p	f_p (THz)	$-G_p$ (10^8 Sm^{-2})	$-Z_{Rp}$ (10^{-9} Ωm^2)	P_{RF} (10^{10} Wm^{-2})	$-Q_P$
4H-SiC (unilluminated)	10^6	10^6	0.325	162.0	2.35	36.90	1.26
4H-SiC (TM)	50	10^6	0.33	158.0	2.30	35.99	1.32
4H-SiC (TM)	25	,,	0.34	156.0	2.29	35.54	1.34
4H-SiC (FC)	10^6	50	0.35	135.0	1.48	30.75	2.0
4H-SiC (FC)	10^6	25	0.37	120.0	1.15	27.33	2.50
6H-SiC (unilluminated)	10^6	10^6	0.35	101.0	1.30	14.99	2.58
6H-SiC (TM)	50	10^6	0.353	99.0	1.12	14.70	2.84
6H-SiC (TM)	25	,,	0.36	96.0	1.03	14.25	2.91
6H-SiC (FC)	10^6	50	0.362	90.0	0.84	13.36	3.50
6H-SiC (FC)	10^6	25	0.38	85.4	0.76	12.68	3.80
3C-SiC (unilluminated)	10^6	10^6	0.353	152.0	1.60	22.99	1.80
3C-SiC (TM)	50	10^6	0.353	150.0	1.50	22.68	1.90
3C-SiC (TM)	25	,,	0.355	149.0	1.44	22.53	1.94
3C-SiC (FC)	10^6	50	0.356	138.6	1.44	20.96	2.0
3C-SiC (FC)	10^6	25	0.360	125.0	1.20	18.91	2.32

Table 4. Optical illumination effects on SiC IMPATTs in the THz regime (frequency = 0.3 THz).

To study the microscopic properties of the devices the authors has computed the spatial distribution of negative resistivity (R(x)) in the depletion layer of the device, which would give an insight into the region of depletion layer that contribute to THz power. The computed R(x) profiles at the respective optimum frequencies fP of the DDRs are shown in figure 14. The computed R(x) profiles in each case is characterized by two negative resistivity peaks (Rmax) in the middle of each drift layer along with a central negative resistivity minimum (Rmin) located near the metallurgical junction. Furthermore, the magnitude of negative resistivity peaks produced by holes in the hole drift layer (Rmax,,p) is appreciably higher compared with the peak produced by electrons in the electron drift layer (Rmax, n). This may be due to the fact that in SiC, hole is more ionizing carrier than electrons [5]. The study also reveals that under normal operating conditions of the DDRs, the values of Rmin is appreciable, which indicates that the central avalanche zone of all the DDR SiC IMPATTs contributes appreciably to the THz power although to a lesser extent than the corresponding drift zone. Some qualitative estimate of the THz-power contributed by the avalanche region of the devices can be obtained from the contribution of the small-signal negative resistance (-ZR) from the avalanche zone, which is the area of the R(x) profile bounded by avalanche zone. The dependence of magnitudes of the negative resistivity peaks in the two drift layers of 4H-SiC, 6H-SiC and 3C-SiC diodes can be explained by considering the relative magnitudes of the ionization rates of electrons and holes in the avalanche zone. It is observed that in case of all the diodes, under optical illumination, the magnitudes of the peaks of the negative resistivity profiles decrease and

their locations shift towards the nn++ and pp++ edges of the drift layer with the decrease of Mn or MP. The depression of the peaks and the shift of the R(x) profiles are less pronounced in TM diode structure (Figure 14) while the same are more pronounced in FC diode structure (Figure 14). The optical illumination studies on the three types of SiC DDRs thus reveals that 4H-SiC based IMPATT is comparatively more photo- sensitive than its counterparts.
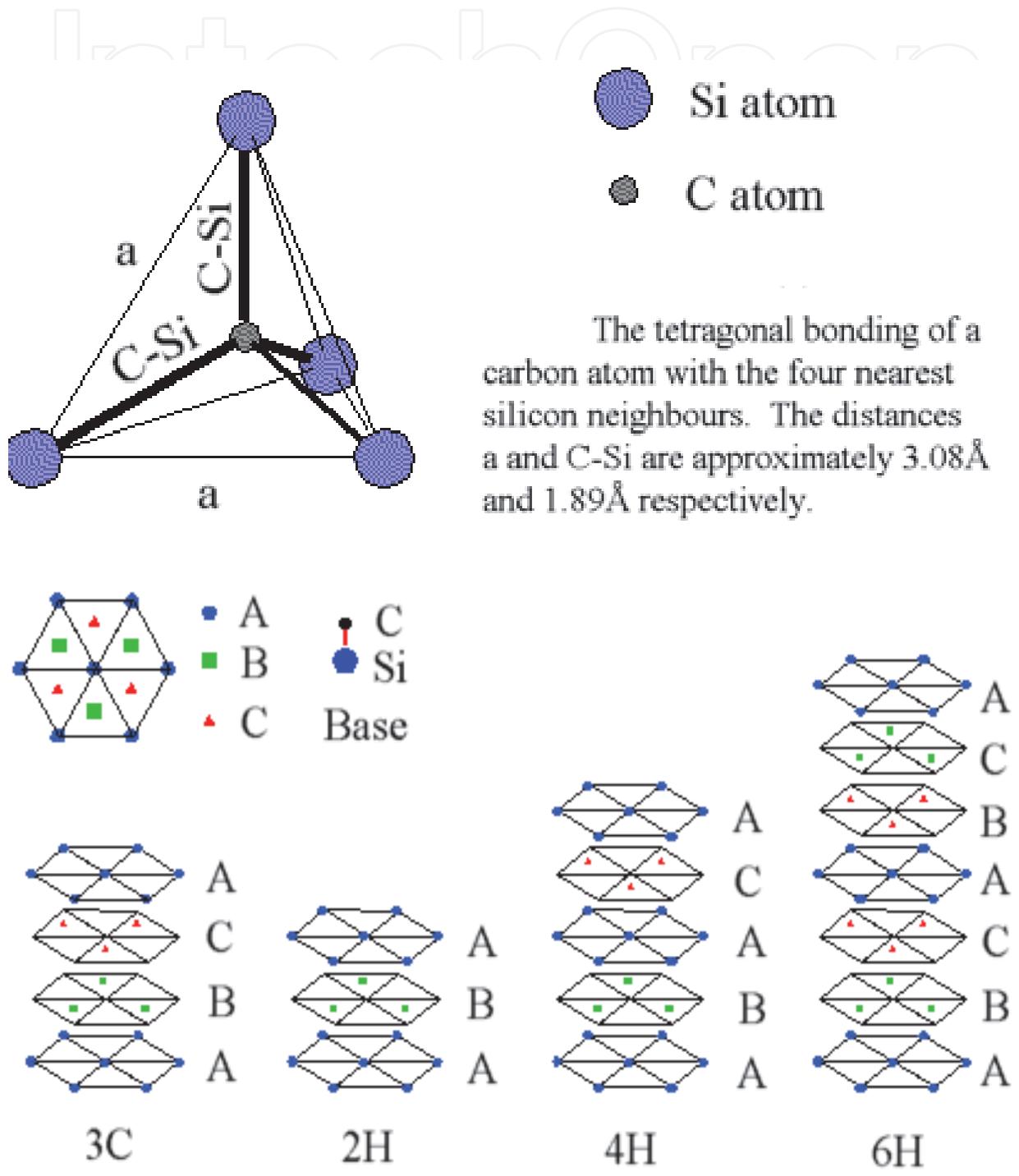
Fig. 8. The stacking sequence of double layers of the three most common SiC polytypes
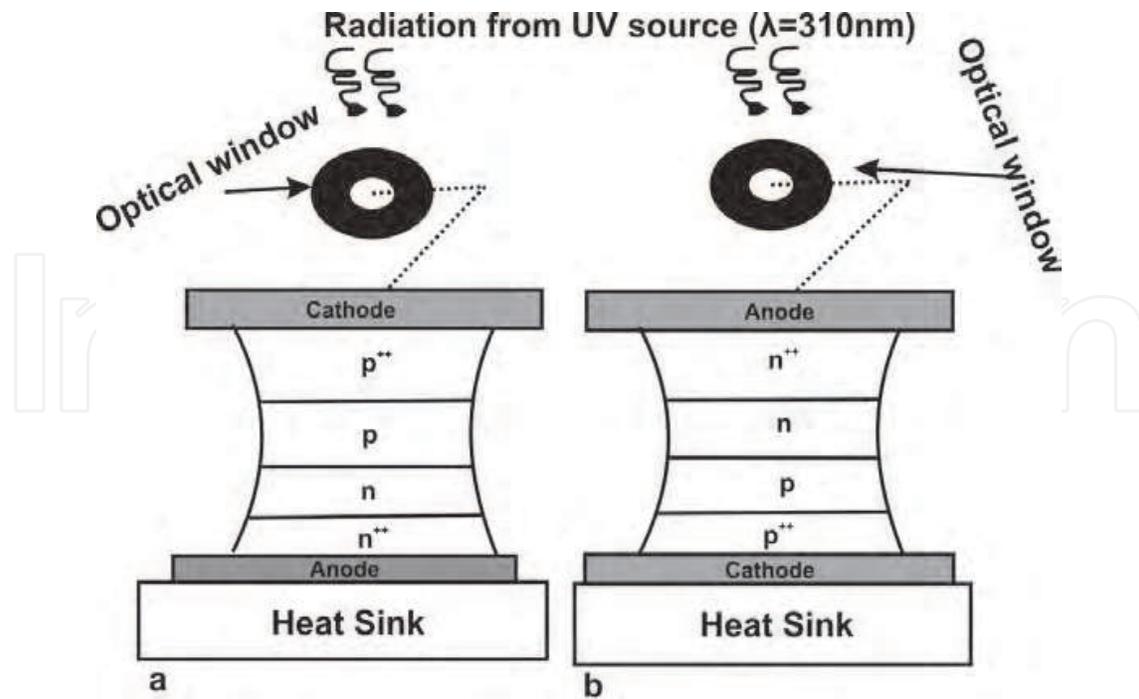
Fig. 9. (a) Top-Mounted IMPATT and (b) Flip-Chip IMPATT
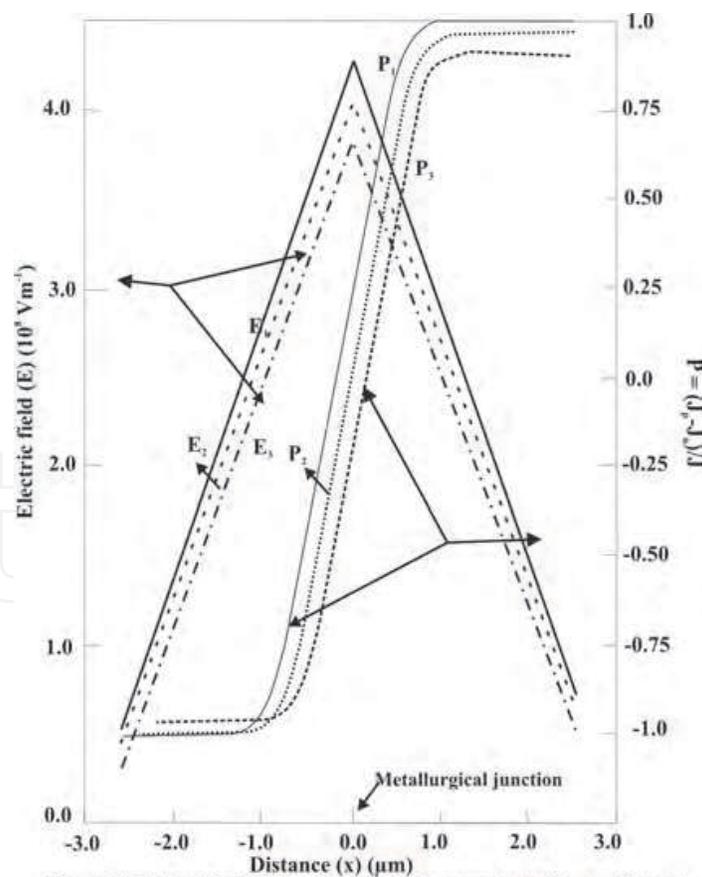
Fig. 10. (a) Electric field and normalised current density profiles of 4H-SiC IMPATT at THz region. E_1 and P_1 are un-illuminated diodes and $E_{2,3}$ and $P_{2,3}$ are illuminated TM ($_2$) and FC ($_3$) diodes.
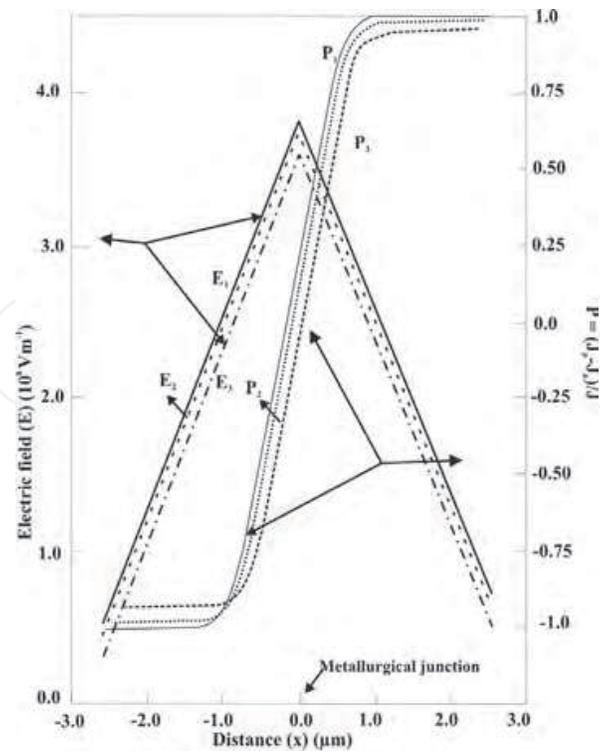
Fig. 10. (b) Electric field and normalised current density profiles of 6H-SiC IMPATT at THz region. E1 and P1 are un-illuminated diodes and E2,3 and P2,3 are illuminated TM (2) and FC (3) diodes.
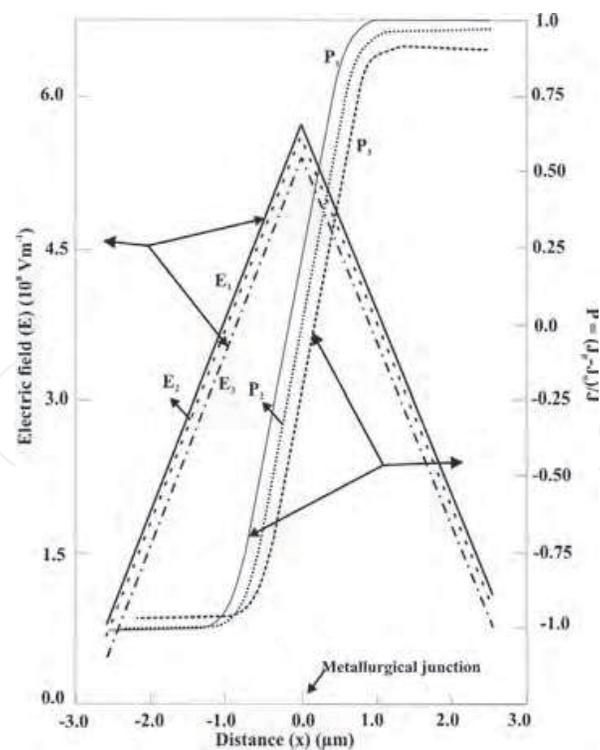
Fig. 10. (c) Electric field and normalised current density profiles of 3C-SiC IMPATT at THz region. E_1 and P_1 are un-illuminated diodes and $E_{2,3}$ and $P_{2,3}$ are illuminated TM ($_2$) and FC ($_3$) diodes.
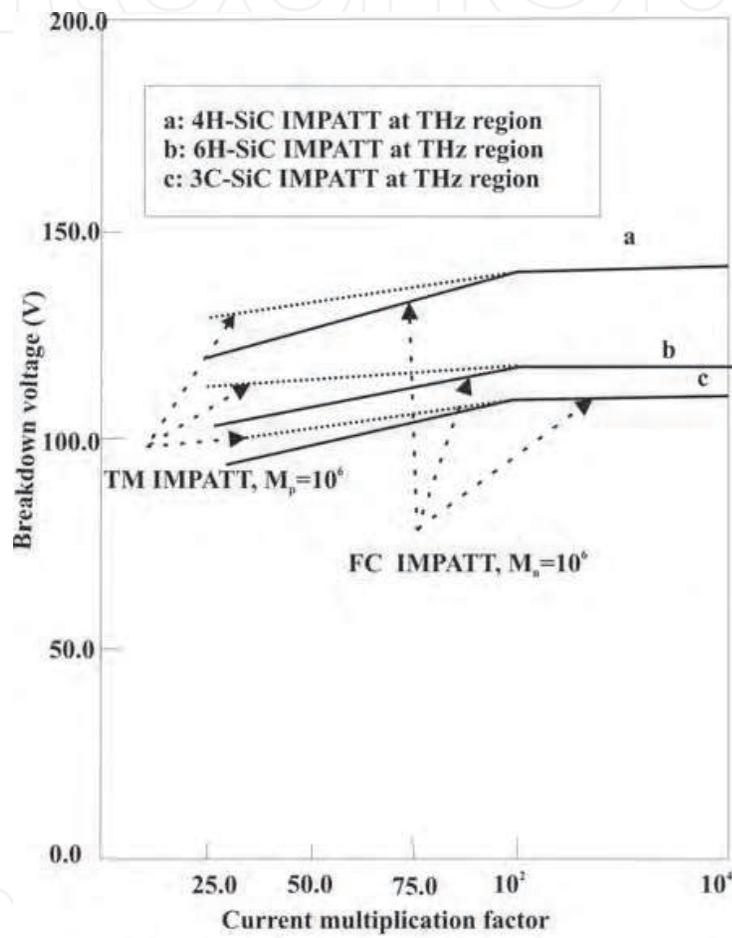
Fig. 11. Plots of breakdown voltage as a function of electron and hole current multiplication factors of SiC THz IMPATTs.
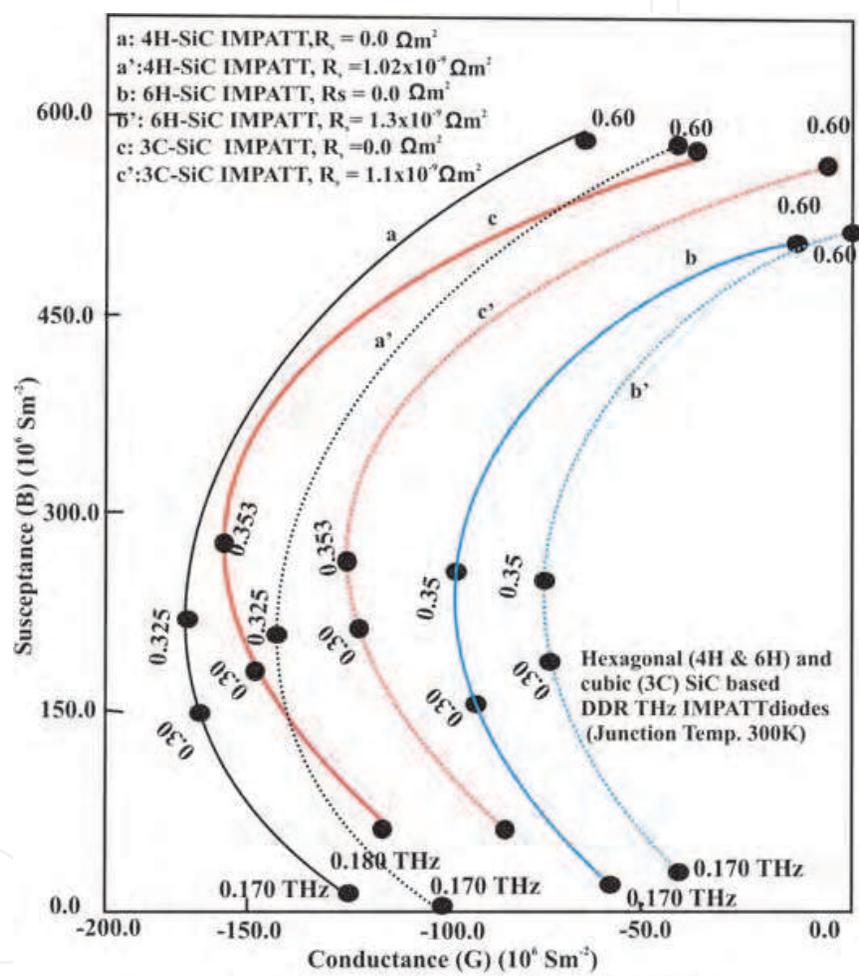
Fig. 12. Admittance plots of SiC DDR IMPATTs in the Terahertz region, dotted lines are incorporating the series resistance effects.

Fig. 13. Effect of photo-illumination on FC and TM illumination configuration of SiC (3C, 4H and 6H type) based terahertz DDR IMPATT diodes at room temperature (300K).
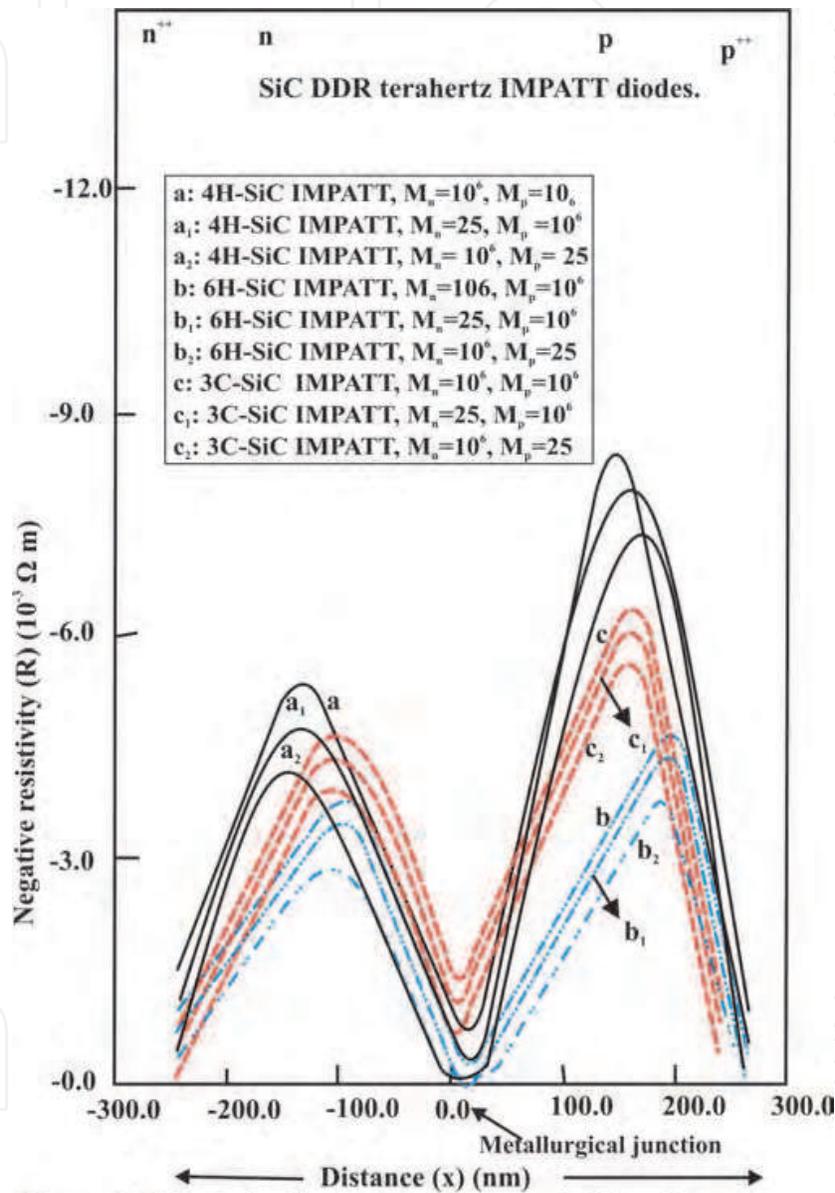
Fig. 14. Effect of radiation on negative resistivity plots of SiC DDR IMPATTs in the Terahertz region.

5. Acknowledgment(s)

The author wish to acknowledge Director, CMSDS, University of Calcutta for providing necessary support to do this work. The author is grateful to (late) Prof. S. K. Roy, Professor and founder Director, CMSDS, University of Calcutta and (late) Prof. Nilratan Mazumder, Professor, West Bengal University of Technology, India for providing their valuable suggestions during this work.

6. References

[1] Mukherjee, M; Mazumder, N; Roy, S.K; and Goswami, K ; "GaN IMPATT diode: A photosensitive high power Terahertz source", Semiconductor Science and Technology, (2007), vol. 22, pp. 1258-1267.

[2] Gummel, H. K; Blue, J.L ; 'A small signal theory of avalanche noise in IMPATT Diodes', IEEE Trans. Electron Devices (1967), vol. 14, p. 569.

[3] Adlerstein, M. G, Holway, Chu, S. L. "Measurement of series resistance in IMPATT diodes", IEEE Trans. Electron Devices, vol. ED- 30, p. 179,.

[4] Mukherjee, M; Mazumder, N; Dasgupta, A; "Effect of Charge Bump on Series Resistance and Ka-Band performance of 4H-SiC IMPATT Oscillator", Proceedings of "IEEE International symposium on Integrated circuits" (IEEE-ISIC 2007), September 26-28, (2007), Nanyang Technological University, and IEEE- Singapore. pp. 61-64

[5] Electronic Archive: New Semiconductor Materials, Characteristics and Properties (Online) www.ioffe.ru/SVA/NSM/Semicond/SiC.
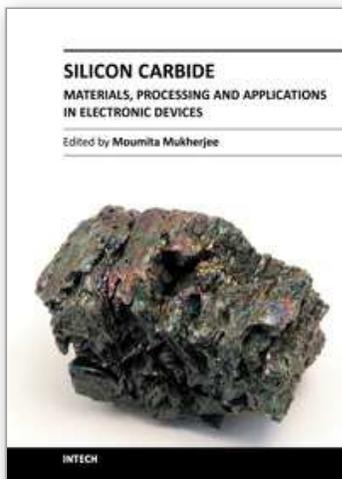
Silicon Carbide - Materials, Processing and Applications in Electronic Devices

Edited by Dr. Moumita Mukherjee

Silicon Carbide (SiC) and its polytypes, used primarily for grinding and high temperature ceramics, have been a part of human civilization for a long time. The inherent ability of SiC devices to operate with higher efficiency and lower environmental footprint than silicon-based devices at high temperatures and under high voltages pushes SiC on the verge of becoming the material of choice for high power electronics and optoelectronics. What is more important, SiC is emerging to become a template for graphene fabrication, and a material for the next generation of sub-32nm semiconductor devices. It is thus increasingly clear that SiC electronic systems will dominate the new energy and transport technologies of the 21st century. In 21 chapters of the book, special emphasis has been placed on the "materials" aspects and developments thereof. To that end, about 70% of the book addresses the theory, crystal growth, defects, surface and interface properties, characterization, and processing issues pertaining to SiC. The remaining 30% of the book covers the electronic device aspects of this material. Overall, this book will be valuable as a reference for SiC researchers for a few years to come. This book prestigiously covers our current understanding of SiC as a semiconductor material in electronics. The primary target for the book includes students, researchers, material and chemical engineers, semiconductor manufacturers and professionals who are interested in silicon carbide and its continuing progression.

INTECH

open science | open minds